coupled susceptibility component that is responsible for the susceptibility temperature dependence through lattice expansion. In some alloys of Ti, the observation that changes in slope of $\chi(T)$ tend to occur at about the same temperatures as changes in the lattice-parameter thermal-expansion coefficients gives some support to this postulate. However, a good experimental test of the influence of lattice expansion on magnetic susceptibility (in particular, χ_{orb}[26]) would be to compare $(\partial\chi/\partial T)_P$ with either $(\partial\chi/\partial T)_V$ or $(\partial\chi/\partial V)_T$.

ACKNOWLEDGMENTS

We wish to acknowledge R. D. Smith and G. W. Waters for technical assistance, and the Battelle-Columbus Laboratories for financial support. We also wish to acknowledge Dr. T. R. Cass for his help in providing us with some very good crystals of Ti and Zr.

[1]E. W. Collings and J. C. Ho, Phys. Rev. B2, 235 (1970).
[2]N. V. Vol'kenshteyn, E. V. Galoshina, and N. I. Shchegolikhina, Fiz. Metal. i Metalloved. 25, 180 (1968).
[3]MARZ-grade material was purchased. The nominal purity of the Zr was 99.99%. That of the Hf was 99.97% for all elements except Zr, which was stated to be present to a nominal concentration of about 3 wt%. All the usual suppliers quote this level of Zr contamination in "high-purity" Hf.
[4]J. C. Ho and R. Viswanathan, Phys. Rev. 172, 705 (1968).
[5]E. W. Collings and R. D. Smith, J. Appl. Phys. 39, 4463 (1968).
[6]Zr-1 was measured in June, 1968 (as were Hf-1 and Hf-2); Zr-2 was measured in January, 1971.
[7]J. Butterworth, Proc. Phys. Soc. (London) 83, 71 (1964).
[8]A. M. Clogston, V. Jaccarino, and Y. Yafet, Phys. Rev. 134, A650 (1964).
[9]S. L. Altmann and C. J. Bradley, Proc. Phys. Soc. (London) 92, 764 (1967).
[10]A. C. Thorsen and A. S. Joseph, Phys. Rev. 131, 2078 (1963).
[11]W. R. Angus, Proc. Roy. Soc. (London) A136, 569 (1932).
[12]P. W. Selwood, *Magnetochemistry* (Interscience, New York, 1956), p. 78.
[13]R. Kubo and Y. Obata, J. Phys. Soc. Japan 11, 547 (1956).
[14]L. E. Orgel, J. Phys. Chem. Solids 21, 123 (1961).
[15]A. M. Clogston, A. C. Gossard, V. Jaccarino, and Y. Yafet, Phys. Rev. Letters 9, 262 (1962).
[16]J. S. Denbigh and W. M. Lomer, Proc. Phys. Soc. (London) 82, 156 (1963).
[17]N. Mori, J. Phys. Soc. Japan 20, 1383 (1965).
[18]N. Mori, J. Phys. Soc. Japan 26, 926 (1969).
[19]W. E. Gardner and J. Penfold, Phil. Mag. 11, 549 (1965).
[20]W. E. Gardner, J. Penfold, and M. A. Taylor, Proc. Phys. Soc. (London) 85, 963 (1965).
[21]In Gardner (Refs. 19, 20) [but not 22], $n(E_F)$ is the total Fermi density of states, so that $\alpha_G = n(E_F)\,\phi$.
[22]W. M. Lomer and W. E. Gardner, Progr. Mater. Sci. 14, 145 (1969).
[23]D. Pines, Solid State Phys. 1, 367 (1955).
[24]W. L. McMillan, Phys. Rev. 167, 331 (1968).
[25]E. W. Collings and J. C. Ho, in *Proceedings of the Third IMR Symposium on Electronic Density of States* (U. S. GPO, Washington, D. C., 1970), Natl. Bur. Std. U. S. Spec. Publ. 323.
[26]The intrinsic volume dependence of χ_P is negligible in this context.

PHYSICAL REVIEW B VOLUME 4, NUMBER 2 15 JULY 1971

Raman Spectra and Lattice Dynamics of Tellurium†

A. S. Pine and G. Dresselhaus
Lincoln Laboratory, Massachusetts Institute of Technology, Lexington, Massachusetts 02173
(Received 5 March 1971)

The Raman spectrum of trigonal tellurium has been obtained at 295 and 90 °K. The Raman-active A_1 singlet and two E doublets are identified by the scattering polarization selection rules, and the E-mode LO-TO splittings and linear wave-vector shifts are observed. The natural linewidths of the phonons are resolved and some weak second-order structure is evident. A spectrum of amorphous tellurium is also presented. The data on trigonal tellurium, together with neutron-scattering and infrared reflectivity measurements, are used to construct a lattice-dynamical model based on a symmetrized Fourier-expansion scheme incorporating generalized noncentral forces.

I. INTRODUCTION

The lattice vibrations of trigonal tellurium have been studied recently by neutron scattering,[1] infrared reflectivity,[2] and Raman scattering.[3,4] The principal Raman modes of $A_1 + 2E$ symmetry have been identified by Pinczuk, Lucovsky, and Burstein[3] and by Torrie.[4] The latter work, however, contains some spurious lines and somewhat inconclusive polarization data. Complementary Raman data are presented here together with a lattice-dynamics calculation of the phonon spectrum. New results

include the doublet E-mode LO-TO splittings and linear wave-vector shifts, the resolved linewidths of the modes, definitive polarization selection rules, and second-order structure. The first-order Raman and infrared data are confined to the center of the Brillouin zone whereas the neutron data are available along the four high-symmetry axes of the full zone. Nevertheless, the Raman measurements are more precise than the others and do yield some phonon-dispersion information for small wave vectors away from the Γ point. The previous phonon symmetry identifications are generally confirmed by the Raman-scattering selection rules, except for the band orderings along the trigonal axis. Anharmonic effects are readily observed in the temperature dependence of the Raman shifts and linewidths. The weak second-order structure is tentatively identified as combination frequencies and overtones based on the neutron measurements and the lattice model. Finally, the spectrum of an amorphous form of tellurium obtained by melting the surface of the crystal with an intense laser beam is discussed.

II. CRYSTAL SYMMETRY AND DYNAMICAL MODELS

Tellurium crystallizes with space group D_3^4 (or D_3^6) having three atoms per unit cell arranged helically about the c axis. The symmetries of the optical phonons at the center of the Brillouin zone are one Raman-active A_1 singlet, one infrared-active (extraordinary ray) A_2 singlet, and two Raman- and infrared-active (ordinary ray) E doublets. Though tellurium is homonuclear, there is a dynamic charge associated with the A_2 and E modes,[5] the s ength of which has been measured in the reststrahlen.[2] This effective charge is also measured in the Raman experiment by the splitting of the E doublet, for wave vector $\vec{q} \perp c$ axis, into modes of longitudinal and transverse polarization. Also, for $\vec{q} \parallel c$ axis, the purely transverse E doublet is split proportional to $\vec{q}$ as a consequence of the screw symmetry of the lattice.[6] This dispersion is measurable by high-resolution Raman scattering since phonon wave vectors of about $4\pi|\eta + i\kappa|/\lambda$ may be probed, where η and κ are the real and imaginary parts, respectively, of the refractive index, and λ is the incident-light wavelength. Such linear wave-vector shifts should give rise to the phenomenon of vibration-induced infrared-optical activity[6] which has not yet been observed.

Lattice-dynamics calculations for trigonal tellurium have been carried out previously by Hulin[7] and Powell and Martel.[1] Hulin endeavored to explain the elastic constants[8] and infrared-absorption[9] data that existed at the time with a simple three-force-constant model. He computed the phonon dispersion only along the trigonal Δ axis. Later Geick and Schröder[10] discovered, in a similar calculation on isomorphous selenium, that the Hulin model contains an instability at the K point of the Brillouin zone. This instability is avoided by Powell and Martel in a model which incorporates central forces out to eighth neighbors. However, their model is still in substantial disagreement with their neutron data, and in fact yields a Δ-axis dispersion remarkably similar to Hulin's. It appears then that longer-range forces do not provide a rapidly convergent fit to the data. In this paper a Fourier-expansion model[11] is used where the range of forces is confined to a distance of one unit cell along the trigonal and binary axes (seventh neighbors) but where as many noncentral forces as are allowed by the lattice symmetry are included. Though this greatly multiplies the number of parameters, the known data can be fit with a convergent series. No attempt is made here to refine the model with a deformable electron cloud—for example, a shell model.[5] Therefore only qualitative statements are made about measurements relying on the ionicity or polarizability of the lattice, such as the infrared strength and the Raman intensity.

The Raman polarizability tensors arising from the deformation potential electron-phonon interaction have been given by Loudon.[12] For D_3 symmetry, where x, y, and z are the binary, bisectrix, and trigonal axes,

$$A_1: \begin{bmatrix} a & . & . \\ . & a & . \\ . & . & b \end{bmatrix}, \quad E(x): \begin{bmatrix} c & . & . \\ . & -c & d \\ . & d & . \end{bmatrix}, \quad E(y): \begin{bmatrix} . & c & -d \\ -c & . & . \\ -d & . & . \end{bmatrix}. \tag{1}$$

Because of the electro-optic effect, these scattering tensors must be modified if an electric field is associated with an ion displacement such as an LO phonon.[12] Thus for a scattering geometry $y(x,x)\bar{y}$, the E_{TO} mode has intensity proportional to $|c|^2$, whereas with $x(y,y)\bar{x}$ the E_{LO} mode has intensity $\propto |c'|^2$ which is an interference between the deformation potential and electro-optic contributions. The standard notation for the scattering geometry represents the incident-light wave vector (incident polarization and the scattered-light polarization) and scattered wave vector. A surface back-scattering geometry is employed since the incident-light energy of ~ 2.4 eV is well above the 0.33-eV band gap in Te.

III. EXPERIMENT

The Raman data are obtained in a standard back-scattering configuration using an argon ion laser, a Spex 1400 tandem spectrometer, and an uncooled

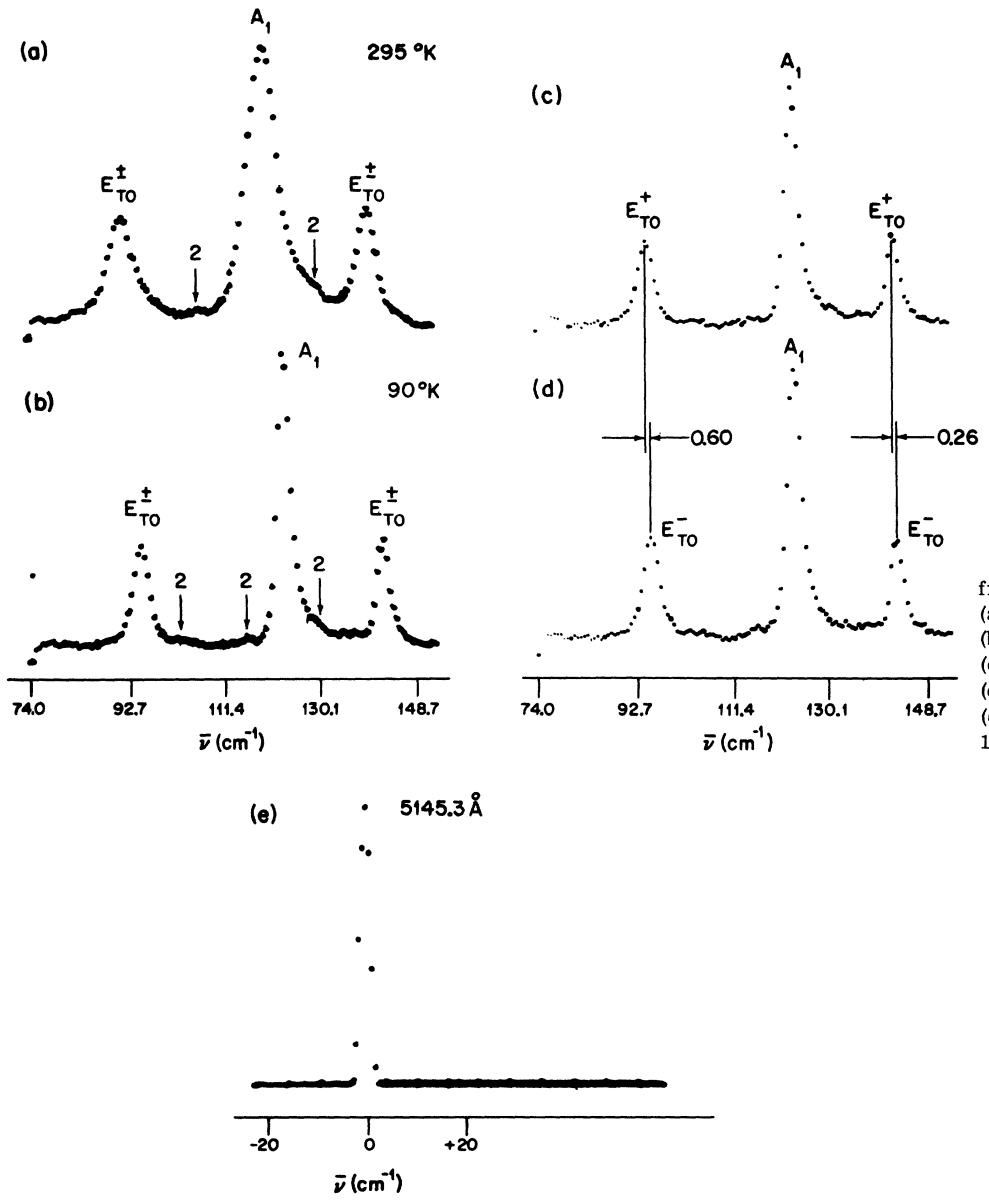

FIG. 1. Raman spectra from tellurium, $\vec{q} \parallel c$ axis; (a) $z(x, x+y)\bar{z}$, 295 °K; (b) $z(x, x+y)\bar{z}$, 90 °K; (c) $z((+), x+y)\bar{z}$, 90 °K; (d) $z((-), x+y)\bar{z}$, 90 °K; (e) instrumental profile, 100-μ slits.

ITT FW130 photomultiplier. Repetitively scanned data are accumulated in a multichannel analyzer to enhance the signal-to-noise ratio. The laser output at 5145 Å is single moded to be used in conjunction with an I_2-vapor absorption filter when the sample surfaces diffusely scatter an excess amount of unshifted light. Laser powers of 100–250 mW are safely focused on tellurium with a 40-mm focal-length cylindrical lens whereas with a 100-mm spherical lens, the sample melts at these power levels.

Tellurium samples obtained from the Alfa, Kennecott, and Xerox Corps. yield indistinguishable spectra. Special preparation is required for each crystallographic face. The surface perpendicular to the trigonal axis, the z face, is string-saw cut and etched with an $H_2O:HCl:CrO_3$ solution; the y face is used as grown or cleaved; the x face is spark-planed and polished in a $Br:CH_3OH$ etch. Laué patterns of these surfaces are very sharp, although the x rays penetrate to a greater depth (~ 5 μ) than the light.

The spectra obtained from the z face are shown in Fig. 1. The room-temperature trace in Fig. 1(a) and the 90 °K (liquid-nitrogen cold-finger Dewar) traces in Figs. 1(b), 1(c), and 1(d) illustrate the thermal anharmonic effects on the shifts and widths of the modes.[13] Figures 1(a) and 1(b) resulted from linearly polarized incident light; Figs. 1(c) and 1(d) from opposite circularly polarized incident light;

the scattered light is unanalyzed. The Raman selection rules in Eq. (1) transformed to a circularly polarized basis such that $E^{\pm}_{TO} \equiv E_{TO}(x \pm iy)$ indicate that E^{+}_{TO} and E^{-}_{TO} scatter their respective circularly polarized light. Thus both scatter simultaneously the incident linear polarization. The A_1 mode appears in all of these configurations. The small shifts observed between the oppositely circular polarized vibrations are manifestations of the linear wave-vector splitting allowed along the Δ axis of the Brillouin zone.[6] Here both E^{-}_{TO} modes shift to higher energy than their respective E^{+}_{TO} modes. This result is at variance with the inverted band interpretation given the neutron data.[1]

The observed linear wave-vector shifts are broadened due to the wave-vector distribution arising from the strong absorption of the incident and scattered light. This distribution of the phonon wave vector q takes the form of a damped Lorentzian

$$q/[(q^2 - q_0^2 - \alpha_0^2)^2 + (2q\alpha_0)^2]$$

assuming a semi-infinite plane boundary condition. Here the optical propagation vector $\frac{1}{2}q_0 = 2\pi\eta/\lambda$ and absorption constant $\frac{1}{2}\alpha_0 = 2\pi\kappa/\lambda$ are taken to be the same for both incident and scattered light. If the optical constants are substantially different at the two wavelengths, then the generalization is simply

$$q_0 = 2\pi[(\eta_i/\lambda_i) + (\eta_s/\lambda_s)]$$

and

$$\alpha_0 = 2\pi[(\kappa_i/\lambda_i + (\kappa_s/\lambda_s)].$$

A direct measurement of the complex refractive index of tellurium at $\lambda = 5145$ Å by the angle-of-incidence reflectivity technique[14] yields $\eta = 2.3 \pm 0.2$ and $\kappa = 3.5 \pm 0.2$. The peak of the above distribution occurs for $q = 4\pi|\eta + i\kappa|/\lambda \simeq 10^6$ cm^{-1} which is about $\frac{1}{50}$ of the Brillouin-zone-edge wave vector. The inhomogeneous broadening of the $E^{\pm}_{TO}$ spectra due to this wave-vector spread is on the order of the splitting which, in turn, is just slightly less than the residual homogeneous lifetime broadening of these modes at 90 °K. In order to observe these small splittings and narrow linewidths, the spectrometer is operated with 100-μ slits yielding the 2-cm^{-1}-broad instrumental profile shown in Fig. 1(e).

In addition to the first-order Raman spectra in Fig. 1, several persistent weak modes of probable second-order origin (labeled 2) are evident. This structure occurs between 100 and 130 cm^{-1}, surprisingly, since the neutron data[1] do not reveal any phonons in the 50–70-cm^{-1} gap. Thus it would appear that combination frequencies (where frequencies are in wave-number units) rather than overtones are responsible for the observed second-order structure. In Sec. V this second-order spectrum is compared to the phonon density of states computed from the lattice-dynamics model described in Sec. IV.

The Raman spectra from the y and x faces are presented in Fig. 2. Here the phonon propagation is normal to the trigonal axis so the E modes are split into longitudinal and transverse branches. Figure 2(a), with geometry $y(x, x+z)\bar{y}$, contains A_1 with strength $|a|^2$, E_{TO} with strength $|c|^2$, and E_{LO} with strength $|d'|^2$. The prime refers to the electro-optic modified scattering tensor component. The lower E_{LO} is not observable since its $|d'|^2$ is unmeasurably small as shown by the $y(x, z)\bar{y}$ trace. The LO-TO splitting for the upper E mode is small but measurable at 90 °K using 100-μ slits. The linewidths of the E modes are slightly sharper here than for the z face since there are no linear wave-vector shifts causing inhomogeneous broadening. There is a negligible effect on the spectrum from the strong phonon dispersion in the polariton region because this region is an insignificant portion of the range of wave vectors probed. Thus the true lifetime-broadened linewidths are deconvolved from the y-face spectra.

The lower E_{LO} mode can be observed with intensity $|c'|^2$ from an x-face sample as shown in Fig. 2. This trace is taken at room temperature with 200-μ slits and an I_2-vapor filter. The I_2 filter is necessary to eliminate the grating ghosts caused by the excessive scattering from this difficult-to-polish surface; unfortunately, it also reduces the Raman-scattered light by a factor of 4. The slits were opened to gather more light since high resolution is unnecessary to observe the large LO shift for the lower E mode. The position of the LO predicted from the measured infrared coupling[2] is labeled IR.

The electro-optic contribution to the scattering intensity $|c'|^2$ may be evaluated by comparing Figs. 1(a) and 2(c). Relative to the A_1 intensity ($|a|^2$ in both traces), it is seen that for the upper E mode $|c'|^2 \sim |c|^2$, whereas for the lower E mode $|c'|^2 \ll |c|^2$. This very weak scattering for the lower E_{LO} indicates an almost complete destructive interference between the electro-optic and deformation potential contributions. However, it should be noted that the anomalous broadening of the line, the discrepancy with the IR measured splitting, and a small residual of "forbidden" E_{TO} scattering may imply a surface-dependent phenomenon. The upper E_{LO} is apparently unaffected by the surface.

A summary of the Raman shifts and natural linewidths (full width at half-maximum) in tellurium at two temperatures is presented in Table I. The widths given are those of Lorentzian lines which, when convolved with the instrumental profile, Fig. 1(e), reproduce the experimental widths. The large percentage errors at 90 °K represent the difficulty in resolving these very sharp lines. A complete

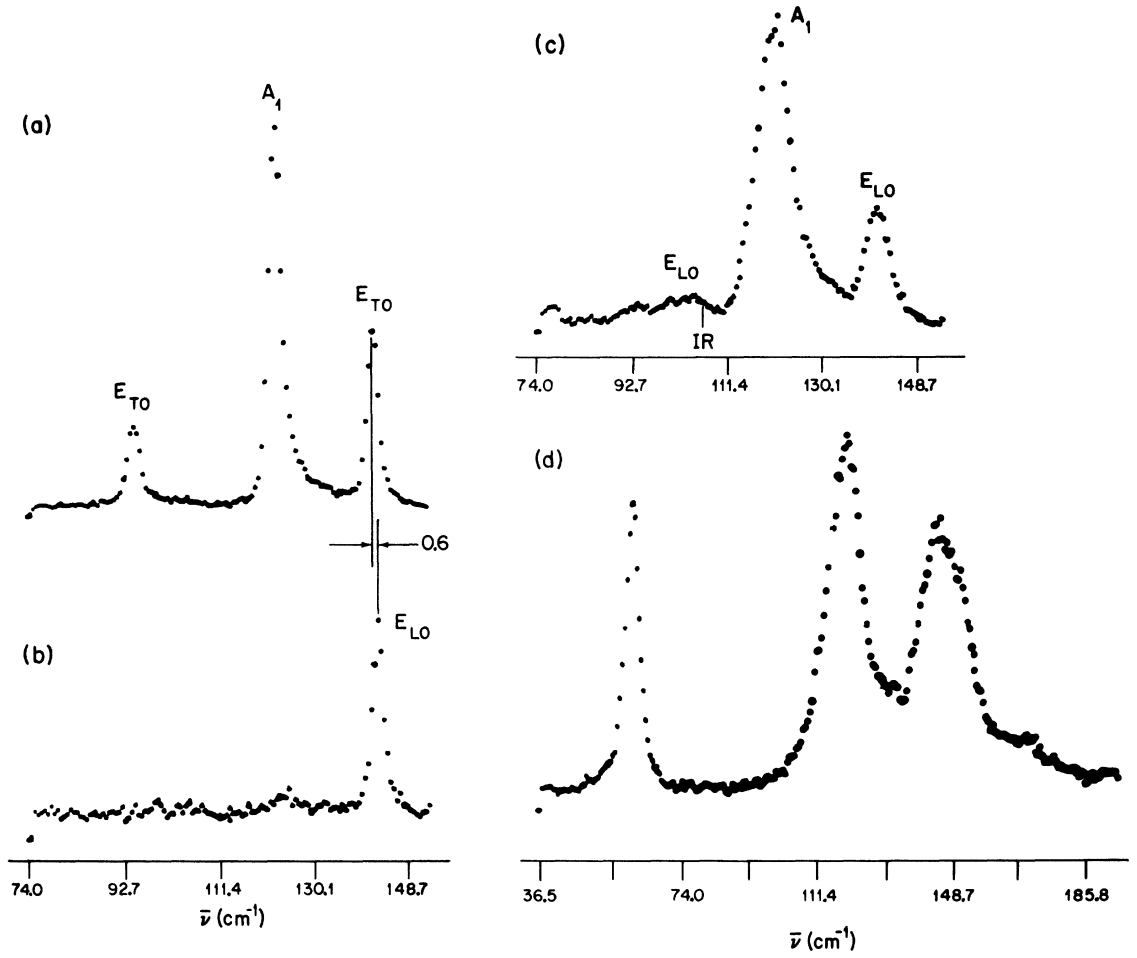

FIG. 2. Raman spectra from tellurium, $\vec{q} \perp c$ axis: (a) $y(x, x+z)\bar{y}$, 90 °K; (b) $y(x, z)\bar{y}$, 90 °K; (c) $x(y, y+z)\bar{x}$, 295 °K; (d) amorphous, 295 °K.

fit to the spectral shape is not attempted, particularly because of the obvious asymmetry of the A_1 mode. The cause of this asymmetry is not clear, though it may arise from a second-order shoulder or a coupled one- and two-phonon anticrossing.[15]

The spectrum obtained from amorphous Te is shown in Fig. 2(d). Here the molten material is created by focusing 125 mW of laser power with a 100-mm spherical lens onto a crystalline z face. The spectrum persists after the melt has resolidified—but not recrystallized—at lower laser power and is independent of the initial face. Spurious lines in the spectrum from the strong diffusion are suppressed by an interference filter before the sample and an I_2-vapor filter after. The three principal bands, peaked at 62, 120, and 146 cm^{-1}, are all completely depolarized and are about two orders of magnitude more intense than the scattering from the crystalline A_1 mode. The depolarization is likely due to scrambling of the incident light by the randomly oriented birefringent chains of Te.

The Raman spectrum from a disordered system with short-range correlation may reflect the single-phonon density of states of the parent crystal, suitably weighted by a frequency dependence and a scattering efficiency.[16] The density of states computed in Sec. V will be compared to this spectrum

TABLE I. Raman-scattering data in tellurium.

Mode	Temperature 295 °K Frequency (cm^{-1})	Linewidth (cm^{-1})	Temperature 90 °K Frequency (cm^{-1})	Linewidth (cm^{-1})
E_{TO}	92.2±0.5	4.8±0.5	95.2±0.5	1.2±0.5
E_{LO}-E_{TO}	12±2	···	···	···
E^{+}_{TO}-E^{-}_{TO}	···	···	−0.60±0.1	···
A_1	120.4±0.5	6.4±0.5	123.4±0.5	1.5±0.5
E_{TO}	140.7±0.5	2.8±0.5	142.9±0.5	0.4±0.4
E_{LO}-E_{TO}	···	···	0.6±0.2	···
E^{+}_{TO}-E^{-}_{TO}	···	···	−0.26±0.1	···

of amorphous tellurium.

IV. FOURIER EXPANSION OF DISPERSION RELATIONS FOR CRYSTALS OF D_3^4 SYMMETRY

The unit cell for crystals with D_3^4 structure contains three atoms (molecules) located at

$$\vec{\tau}_1 = (ra, 0, 0), \quad \vec{\tau}_2 = (-\tfrac{1}{2}ra, \tfrac{1}{2}\sqrt{3}ra, \tfrac{1}{3}c),$$

$$\vec{\tau}_3 = (-\tfrac{1}{2}ra, -\tfrac{1}{2}\sqrt{3}ra, \tfrac{2}{3}c),$$

where for tellurium $a = 4.45$ Å, $c = 5.93$ Å, and $r = 0.269$. An r of 0.5 would correspond to D_6^5 symmetry. In order to construct a dynamical matrix which displays the crystal symmetry, it is convenient to use as basis functions the lattice displacements

$$U_\mu^{(0)}(\vec{q}) = (3N)^{-1/2} \sum_l \{e^{i\vec{q}\cdot\vec{R}_l}[e^{i\vec{q}\cdot\vec{\tau}_1} u_\mu(\vec{R}_l + \vec{\tau}_1) + e^{i\vec{q}\cdot\vec{\tau}_2} u_\mu(\vec{R}_l + \vec{\tau}_2) + e^{i\vec{q}\cdot\vec{\tau}_3} u_\mu(\vec{R}_l + \vec{\tau}_3)]\}, \quad (2a)$$

$$U_\mu^{(1)}(\vec{q}) = U_\mu^{(0)}(\vec{q} + (2\pi/c)(0, 0, 1)), \quad (2b)$$

$$U_\mu^{(2)}(\vec{q}) = U_\mu^{(0)}(\vec{q} + (4\pi/c)(0, 0, 1)). \quad (2c)$$

Here N is the number of unit cells; the $\vec{R}_l$ are the lattice vectors of the hexagonal Bravais lattice of D_{6h} symmetry; u_μ are the individual atomic displacements; and μ is the polarization subscript representing

$$\{z, +, -\} \equiv z, \frac{x+iy}{\sqrt{2}}, \frac{x-iy}{\sqrt{2}}.$$

Although these basis functions serve to establish the desired symmetry relations, the normal modes that are determined by this method are independent of the specific choice of basis functions, provided they exhibit the proper symmetry characteristics. To describe the coupling between these basis functions for a crystal with the first two structure factors vanishing at the hexagonal Brillouin-zone faces, it is necessary to consider a 9×9 dynamical matrix of the form

$$D_{A_1}(\vec{q}) = \begin{bmatrix} D_{A_1}^{(0)}(\vec{q}) & [D_E^{(2)}(\vec{q})]^\dagger & D_E^{(1)}(\vec{q}) \\ D_E^{(2)}(\vec{q}) & D_{A_1}^{(1)}(\vec{q}) & [D_E^{(0)}(\vec{q})]^\dagger \\ [D_E^{(1)}(\vec{q})]^\dagger & D_E^{(0)}(\vec{q}) & D_{A_1}^{(2)}(\vec{q}) \end{bmatrix}, \quad (3)$$

where the submatrices $D_{\Gamma_i}^{(l)}(\vec{q})$ are 3×3 matrices related by

$$D_{\Gamma_i}^{(l)}(\vec{q}) = D_{\Gamma_i}^{(0)}(\vec{q} + (2\pi l/c)(0, 0, 1)), \quad (4)$$

and the dagger in Eq. (3) denotes the Hermitian transpose. The eigenvalues ω^2 of the dynamical matrix obtained from the secular equation

$$|D_{A_1}(\vec{q}) - \omega^2 \overleftrightarrow{1}| = 0 \quad (5)$$

yield the angular frequencies ω of the normal modes for wave vector $\vec{q}$. The dynamical matrix is invariant under time reversal and under all symmetry operations of the space group which is signified by the A_1 symmetry designation.

The q_z translational relations, Eq. (4), due to the threefold screw symmetry reduces the problem to consideration of only two fundamentally distinct submatrices, namely, $D_{A_1}^{(0)}(\vec{q})$ and $D_E^{(0)}(\vec{q})$. The submatrix $D_{A_1}^{(0)}(\vec{q})$ has A_1 symmetry when referred to the proper point-group symmetry of the tellurium lattice D_3. On the other hand, when referred to the point-group symmetry displayed by the hexagonal Bravais lattice D_{6h}, the A_1 symmetry is derived from the A_{1g}, A_{1u}, B_{1g}, B_{1u} symmetry types. Similarly the interaction matrix $D_E^{(0)}(\vec{q})$, which corresponds to the two-dimensional E representation of the group D_3, is derived from the E_{2g}, E_{2u}, E_{1g}, E_{1u} representations of the group D_{6h}. Therefore the submatrices can all be decomposed into

$$D_{A_1}^{(l)}(\vec{q}) = D_{A_{1g}}^{(l)}(\vec{q}) + D_{A_{1u}}^{(l)}(\vec{q}) + D_{B_{1g}}^{(l)}(\vec{q}) + D_{B_{1u}}^{(l)}(\vec{q}), \quad (6a)$$

$$D_E^{(l)}(\vec{q}) = D_{E_{2g}}^{(l)}(\vec{q}) + D_{E_{2u}}^{(l)}(\vec{q}) + D_{E_{1g}}^{(l)}(\vec{q}) + D_{E_{1u}}^{(l)}(\vec{q}), \quad (6b)$$

where the subscripts on the right-hand side label the D_{6h} symmetry of the submatrix for $l = 0$. When $l = 1$ or 2, the symmetry types of the submatrices are mixed, but new labels are unnecessary.

Each of the 3×3 submatrices can be constructed from a basis of nine linearly independent matrices such as

$$J_z = \begin{bmatrix} 0 & 0 & 0 \\ 0 & 1 & 0 \\ 0 & 0 & -1 \end{bmatrix}, \quad \{A_{2g}\} \quad (7a)$$

$$J_+ = \begin{bmatrix} 0 & -1 & 0 \\ 0 & 0 & 0 \\ 1 & 0 & 0 \end{bmatrix}, \quad \{E_{1g}\} \quad (7b)$$

$$J_- = \begin{bmatrix} 0 & 0 & 1 \\ -1 & 0 & 0 \\ 0 & 0 & 0 \end{bmatrix}, \quad \{E_{1g}^*\}, \quad (7c)$$

$$\tfrac{1}{2}[(J_+J_- + J_-J_+) - J_z^2], \quad \{A_{1g}\}, \quad (7d)$$

$$J_z^2, \quad \{A_{1g}\}, \quad (7e)$$

$$-J_-^2, \quad \{E_{2g}\}, \quad (7f)$$

$$-J_+^2, \quad \{E_{2g}^*\}, \quad (7g)$$

$$i[J_zJ_+ + J_+J_z], \quad \{E_{1g}\}, \quad (7h)$$

$$-i(J_zJ_- + J_-J_z), \quad \{E_{1g}^*\}. \quad (7i)$$

The fundamental matrices of Eqs. (7a), (7b), and (7c) are representations of the angular momentum operator $\vec{J} = \vec{r}\times\vec{p}$ for $J = 1$ in the basis $\{z, +, -\}$. They satisfy the usual rules $\vec{J}\cdot\vec{J} = J(J+1)$ and $\vec{J}\times\vec{J} = i\vec{J}$.

These matrices are not unique but are chosen for their symmetry-transformation properties as indicated by their corresponding irreducible representations in the curly brackets and where the two-dimensional representations have a pair of basis functions E and E^*.

The invariance of $D_{A_1}(\vec{q})$ is assured if the $l=0$ submatrices of Γ_i symmetry are constructed from a linear combination of Γ_j symmetry angular momentum basis matrices with functions of the wave vector that transform according to Γ_k such that $\Gamma_j \times \Gamma_k$ contains Γ_i. In addition the $l=0$ subblocks must be time reversal invariant. Thus odd functions of $\vec{q}$ can combine only with the linear J_i, whereas even functions of $\vec{q}$ can combine only with the bilinear J matrices [Eqs. (7d)–(7i)] since both $\vec{q}$ and $\vec{J}$ change signs under time inversion. In this way the submatrices (6a) and (6b) are written

$$D^{(l)}_{A_{1g}}(\vec{q}) = \begin{bmatrix} a^{(l)}_{11}(A_{1g}) & -ia^{(l)}_{12}(E^*_{1g}) & ia^{(l)}_{12}(E_{1g}) \\ ia^{(l)}_{12}(E^*_{1g}) & a^{(l)}_{22}(A_{1g}) & a^{(l)}_{23}(E^*_{2g}) \\ -ia^{(l)}_{12}(E^*_{1g}) & a^{(l)}_{23}(E_{2g}) & a^{(l)}_{22}(A_{1g}) \end{bmatrix}, \tag{8a}$$

$$D^{(l)}_{A_{1u}}(\vec{q}) = \begin{bmatrix} 0 & -a^{(l)}_{12}(E^*_{1u}) & a^{(l)}_{12}(E_{1u}) \\ -a^{(l)}_{12}(E_{1u}) & a^{(l)}_{22}(A_{2u}) & 0 \\ a^{(l)}_{12}(E^*_{1u}) & 0 & -a^{(l)}_{22}(A_{2u}) \end{bmatrix}, \tag{8b}$$

$$D^{(l)}_{B_{1g}}(\vec{q}) = D^{(l)}_{(A_{1g}\times B_{1g})}(\vec{q}), \tag{8c}$$

$$D^{(l)}_{B_{1u}}(\vec{q}) = D^{(l)}_{(A_{1u}\times B_{1g})}(\vec{q}), \tag{8d}$$

$$D^{(l)}_{E_{2g}}(\vec{q}) = \begin{bmatrix} b^{(l)}_{11}(E_{2g}) & -ib^{(l)}_{12}(B_{1g}) + b^{(l)}_{12}(B_{2g}) & ib^{(l)}_{13}(E^*_{1g}) \\ ib^{(l)}_{13}(E^*_{1g}) & b^{(l)}_{22}(E_{2g}) & b^{(l)}_{23}(A_{1g}) + ib^{(l)}_{23}(A_{2g}) \\ -ib^{(l)}_{12}(B_{1g}) + b^{(l)}_{12}(B_{2g}) & b^{(l)}_{32}(E^*_{2g}) & b^{(l)}_{22}(E_{2g}) \end{bmatrix}, \tag{8e}$$

$$D^{(l)}_{E_{2u}}(\vec{q}) = \begin{bmatrix} 0 & -b^{(l)}_{12}(B_{1u}) - ib^{(l)}_{12}(B_{2u}) & b^{(l)}_{13}(E^*_{1u}) \\ -b^{(l)}_{13}(E^*_{1u}) & ib^{(l)}_{22}(E_{2u}) & 0 \\ b^{(l)}_{12}(B_{1u}) + ib^{(l)}_{12}(B_{2u}) & 0 & -ib^{(l)}_{22}(E_{2u}) \end{bmatrix}, \tag{8f}$$

$$D^{(l)}_{E_{1g}}(\vec{q}) = D^{(l)}_{(E_{2g}\times B_{1g})}(\vec{q}), \tag{8g}$$

$$D^{(l)}_{E_{1u}}(\vec{q}) = D^{(l)}_{(E_{2u}\times B_{1g})}(\vec{q}). \tag{8h}$$

Here the notation $D^{(l)}_{(\Gamma_i\times\Gamma_j)}(\vec{q})$ indicates that every irreducible representation that appears in the matrix elements of (8a), (8b), (8e), or (8f) is replaced by the direct product of Γ_i with Γ_j; for example,

$$[D^{(l)}_{E_{1u}}(\vec{q})]_{13} = b^{(l)}_{13}(E^*_{1u}\times B_{1g}) = b^{(l)}_{13}(E^*_{2u}).$$

The matrix elements are given in terms of sums over the symmetrized Fourier functions of the wave vector,

$$a^{(l)}_{ij}(\Gamma_k) = \sum_{mnp} \alpha^{mnp}_{ij}(\Gamma_k) F^{(l)}_{mnp}(\Gamma_k, \vec{q}), \tag{9a}$$

$$b^{(l)}_{ij}(\Gamma_k) = \sum_{mnp} \beta^{mnp}_{ij}(\Gamma_k) F^{(l)}_{mnp}(\Gamma_k, \vec{q}). \tag{9b}$$

Time-inversion symmetry requires all the parameters, α and β, to be real numbers. The complex notation for the symmetry species in the matrix elements refers only to the Fourier function, e.g.,

$$b^{(l)}_{ij}(\Gamma^*_k) = \sum_{mnp} \beta^{mnp}_{ij}(\Gamma_k)[F^{(l)}_{mnp}(\Gamma_k, \vec{q})]^*.$$

The Fourier coefficients, α and β, are the force-constant parameters of the model and the integers m, n, and p denote the range of the forces, establishing the link between any atom and the lattice site $(na, \sqrt{3}pa, \frac{1}{3}mc)$ away.

The symmetrized Fourier functions F are constructed to be periodic in the Brillouin zone, exhibiting the indicated symmetry character for $l=0$. For the general lattice point $(na, \sqrt{3}pa, \frac{1}{3}mc)$ there

is a Fourier function for every irreducible representation of the group D_{6h} including two for each E representation. In the application considered here, however, the expansion converges with the range of the forces restricted to one unit cell along the binary axis ($n \leq 1$) and one unit cell along the trigonal axis ($m \leq 3$). The longer range forces associated with $p \neq 0$ are neglected and the index p is suppressed in what follows. The symmetrized Fourier functions of the wave vector for the lattice site $(na, 0, \frac{1}{3}mc)$ are then given by

$$F_{mn}^{(1)}(A_{1g}, \vec{q}) = C_m^{(1)}(\zeta)[\cos n\xi + \cos\tfrac{1}{2}n(-\xi+\xi') + \cos\tfrac{1}{2}n(-\xi-\xi')], \quad (10a)$$

$$F_{mn}^{(1)}(A_{2u}, \vec{q}) = S_m^{(1)}(\zeta)[\cos n\xi + \cos\tfrac{1}{2}n(-\xi+\xi') + \cos\tfrac{1}{2}n(-\xi-\xi')], \quad (10b)$$

$$F_{mn}^{(1)}(B_{1u}, \vec{q}) = C_m^{(1)}(\zeta)[\sin n\xi + \sin\tfrac{1}{2}n(-\xi+\xi') + \sin\tfrac{1}{2}n(-\xi-\xi')], \quad (10c)$$

$$F_{mn}^{(1)}(B_{2g}, \vec{q}) = S_m^{(1)}(\zeta)[\sin n\xi + \sin\tfrac{1}{2}n(-\xi+\xi') + \sin\tfrac{1}{2}n(-\xi-\xi')], \quad (10d)$$

$$F_{mn}^{(1)}(E_{2g}, \vec{q}) = C_m^{(1)}(\zeta)[\cos n\xi + \Omega\cos\tfrac{1}{2}n(-\xi+\xi') + \Omega^*\cos\tfrac{1}{2}n(-\xi-\xi')], \quad (10e)$$

$$F_{mn}^{(1)}(E_{2u}, \vec{q}) = iS_m^{(1)}(\zeta)[\cos n\xi + \Omega\cos\tfrac{1}{2}n(-\xi+\xi') + \Omega^*\cos\tfrac{1}{2}n(-\xi-\xi')], \quad (10f)$$

$$F_{mn}^{(1)}(E_{1u}, \vec{q}) = C_m^{(1)}(\zeta)[\sin n\xi + \Omega\sin\tfrac{1}{2}n(-\xi+\xi') + \Omega^*\sin\tfrac{1}{2}n(-\xi-\xi')], \quad (10g)$$

$$F_{mn}^{(1)}(E_{1g}, \vec{q}) = iS_m^{(1)}(\zeta)[\sin n\xi + \Omega\sin\tfrac{1}{2}n(-\xi+\xi') + \Omega^*\sin\tfrac{1}{2}n(-\xi-\xi')], \quad (10h)$$

where $\zeta = cq_z$, $\xi = aq_x$, $\xi' = \sqrt{3}aq_y$, $\Omega = e^{2\pi i/3}$, $C_m^{(1)}(\zeta) = \cos\frac{1}{3}m(\zeta + 2\pi l)$, $S_m^{(1)}(\zeta) = \sin\frac{1}{3}m(\zeta + 2\pi l)$. For this restricted case there are no Fourier functions of A_{1u}, A_{2g}, B_{1g}, or B_{2u} symmetry types.

The symmetrized form of the dynamical matrix, [Eq. (3)] for the D_3^4 lattice is now completely defined. Equation (3) also represents the most general form of the Hermitian matrix for the dispersion relations of the electronic p states in tellurium[17] (or selenium). All the additional degeneracies of levels resulting from the vanishing structure factors for this lattice are contained implicitly. This is illustrated in Appendix A where the factorization of the dynamical matrix along the two trigonal axes, Δ and P, is demonstrated. These two axes, with identical point-group symmetry, are nevertheless distinguishable under time-inversion symmetry. In the case of the electronic levels in Te, this leads to the assignment of the valence-band extrema along the P axis,[18] rather than the Δ axis, based on experimental evidence.

The generalization of the dynamical matrix to a molecular or multicomponent D_3^4 lattice such as α-quartz (α-SiO_2) and cinnabar (α-HgS) or a shell model is straightforward. For k sublattices (ions + shells per molecule) the dynamical matrix may be divided up into a $k \times k$ array of 9×9 submatrices. These submatrices are all derivable from the form of $D_{A_1}(\vec{q})$ [Eq. (3)] if the reduced sublattice basis functions are properly symmetrized. For example, the dynamical matrix for α-quartz is given by

$$D(\alpha\text{-}SiO_2) = \begin{bmatrix} [D_{A_1}(\vec{q})]_{kk} & [D_{A_1'}(\vec{q})]_{kk'} & [D_{A_2''}(\vec{q})]_{kk''} \\ [D_{A_1'}(\vec{q})]_{kk'}^{\dagger} & [D_{A_1}(\vec{q})]_{k'k'} & [D_{A_2''}(\vec{q})]_{k'k''} \\ [D_{A_2''}(\vec{q})]_{kk''}^{\dagger} & [D_{A_2''}(\vec{q})]_{k'k''}^{\dagger} & [D_{A_1}(\vec{q})]_{k''k''} \end{bmatrix}, \quad (11)$$

where k labels the Si ion motion, k' is the symmetric combination O + O′ of oxygen motion, and k'' is the antisymmetric combination O − O′. The 9×9 matrices $D_{A_1'}(\vec{q})$ and $D_{A_2''}(\vec{q})$ are derived from $D_{A_1}(\vec{q})$ by crossing every D_{6h} irreducible representation in Eqs. (6) and (8) according to $A_1' = A_1 \times (A_{1g} + A_{1u})$ and $A_2'' = A_1 \times (B_{2g} + B_{2u})$. The simpler two-sublattice case of cinnabar (or tellurium shell model) requires only the 2×2 k and k' subblock of Eq. (11), where k refers to the Hg (or core) motion and k' the S (or shell) motion. Another special case of the formalism occurs for D_6^5 symmetry (e.g., β-quartz). This higher symmetry allows a reduction in the number of independent matrix elements since Eqs. (6a) and (6b) are truncated according to

$$D_{A_1}^{(1)}(\vec{q}) = D_{A_{1g}}^{(1)}(\vec{q}) + D_{A_{1u}}^{(1)}(\vec{q}), \quad (12a)$$

$$D_E^{(1)}(\vec{q}) = D_{E_{2g}}^{(1)}(\vec{q}) + D_{E_{2u}}^{(1)}(\vec{q}), \quad (12b)$$

for D_6^5. Returning now to the lattice vibrational problem in tellurium, some additional constraints must be imposed on the dynamical matrix to ensure uniform translational invariance and lattice stability. The first constraint is specified by

$$D_{A_1}^{(0)}(0) = [D_E^{(2)}(0)]^{\dagger} = D_E^{(1)}(0) = 0, \quad (13)$$

which implies that the acoustic branch frequencies must vanish at $\vec{q} = 0$. Furthermore, for the lattice to be stable, it is necessary that all terms linear in $\vec{q}$ vanish for the acoustic modes. This implies

$$\nabla_q D_{A_1}^{(0)}(\vec{q})\big|_{\vec{q}=0} = 0 \ . \tag{14}$$

Otherwise the eigenvalues for the shear-wave doublet propagating along the c axis would be $\omega^2 \sim \pm q_z$.

In order to make contact with the measured elastic constants, the dynamical matrix is expanded in a Taylor series for small $\vec{q}$. Thus each of the 3×3 submatrices in Eq. (3) takes the form

$$D_{A_1}^{(1)}(\vec{q}) \simeq D_{A_1}^{(1)}(0) + \vec{q}\cdot[\nabla_q D_{A_1}^{(1)}(\vec{q})]_0 + \tfrac{1}{2}\vec{q}\vec{q}:[\nabla_q \nabla_q D^{(1)}(\vec{q})]_0 + \cdots \ , \tag{15a}$$

$$D_E^{(1)}(\vec{q}) \simeq D_E^{(1)}(0) + \vec{q}\cdot[\nabla_q D_E^{(1)}(\vec{q})]_0 + \cdots \ . \tag{15b}$$

The constraints (13) and (14) greatly simplify the dynamical matrix which can be written to lowest nonvanishing powers of $\vec{q}$ as

$$\begin{bmatrix} \tfrac{1}{2}\vec{q}\vec{q}:[\nabla_q\nabla_q D_{A_1}^{(0)}(\vec{q})]_0 - \omega^2\overleftrightarrow{1} & \vec{q}\cdot[\nabla_q D_E(\vec{q})]_0 \\ \vec{q}\cdot[\nabla_q D_E^{\dagger}(\vec{q})]_0 & D_{\rm opt} - \omega^2\overleftrightarrow{1} \end{bmatrix} = 0 \ , \tag{16}$$

where $D_E(\vec{q})$ is the 3×6 matrix,

$$D_E(\vec{q}) = [[D_E^{(2)}(\vec{q})]^{\dagger}, \ D_E^{(1)}(\vec{q})] \ , \tag{17a}$$

and $D_{\rm opt}$ is the 6×6 matrix for the optical modes

$$D_{\rm opt} = \begin{bmatrix} D_{A_1}^{(1)}(0) & [D_E^{(0)}(0)]^{\dagger} \\ D_E^{(0)}(0) & D_{A_1}^{(2)}(0) \end{bmatrix} . \tag{17b}$$

At $q = 0$, the optical eigenmodes are obtained by diagonalizing $D_{\rm opt}$ with a unitary transformation $U_{\rm opt}$ such that

$$U_{\rm opt} D_{\rm opt} U_{\rm opt}^{-1} = \omega_{\Gamma_k}^2 \delta_{jk} \ . \tag{18}$$

Then the secular equation (16) may be written

$$|\vec{q}\vec{q}:\overleftrightarrow{C} - \rho\omega^2\overleftrightarrow{1}| = 0 \ , \tag{19}$$

where the 3×3 elastic constant matrix $\overleftrightarrow{C}$ is given by

$$\overleftrightarrow{C}/\rho = \tfrac{1}{2}[\nabla_q\nabla_q D_{A_1}^{(0)}(\vec{q})]_0 - [\nabla_q D_E(\vec{q})]_0 U_{\rm opt}^{-1}(\delta_{jk}/\omega_{\Gamma_k}^2) U_{\rm opt}[\nabla_q D_E^{\dagger}(\vec{q})]_0 \ . \tag{20}$$

The second term on the right-hand side of (20) represents the interaction of the Γ-point optical and acoustical modes as discussed previously by Miller and Axe.[19] The diagonalization of the optical dynamical matrix allows this perturbation to be written as a sum over the zone-center optical eigenmodes. Miller and Axe[19] demonstrate that only Raman-active modes contribute to this sum.

The secular equation for the acoustic modes (19) can be written in the general symmetry-allowed form

$$\vec{q}\vec{q}:\overleftrightarrow{C} = \mathcal{C}(\vec{q}) \ , \tag{21a}$$

such that the Hermitian matrix $\mathcal{C}(\vec{q})$ has matrix elements

$$\mathcal{C}_{11} = c_{33} q_z^2 + c_{44} q_+ q_- \ , \tag{21b}$$

$$\mathcal{C}_{12} = (1/\sqrt{2})(c_{13} + c_{44}) q_z q_- - (i/\sqrt{2})\, c_{14} q_+^2 \ , \tag{21c}$$

$$\mathcal{C}_{13} = \mathcal{C}_{12}^{*} \ , \tag{21d}$$

$$\mathcal{C}_{22} = c'_{44} q_z^2 + \tfrac{1}{4}(3c_{11} - c_{12}) q_+ q_- \ , \tag{21e}$$

$$\mathcal{C}_{23} = 2i\, c'_{14} q_z q_- + \tfrac{1}{4}(c_{11} + c_{12}) q_+^2 \ , \tag{21f}$$

$$\mathcal{C}_{33} = \mathcal{C}_{22} \ , \tag{21g}$$

where $q_{\pm} = q_x \pm i q_y$. This follows from the definitions (20), (8), and (9) and expansions of the Fourier functions (10). The c_{ij} coefficients are expressed in standard Voigt notation to conform to the measured elastic constants. In this symmetrized model the primed elastic constants are distinct from the corresponding unprimed constants. However, infinitesimal rotational invariance, as discussed by Lax,[20] would imply that the shear indices of the elastic constants are symmetric, hence $c'_{44} = c_{44}$ and $c'_{14} = c_{14}$.

V. LATTICE-MODEL RESULTS AND COMPARISON WITH EXPERIMENTS

The present Raman experiments, augmented by the recently measured inelastic neutron scattering,[1] the infrared reflectivity,[2] and the acoustic measurements of the elastic constants[3] provide a great deal of information on the phonon dispersion of tellurium in high-symmetry regions of the Brillouin zone. The existing lattice models[1,7] inadequately represent these data throughout the zone, even though central forces out to eighth neighbors[1] are considered. In Sec. III, the most general form of the dynamical matrix based on the symmetry of the lattice is written as a Fourier expansion in reciprocal-lattice space. The coefficients of this expansion are determined from experiments and not by recourse to any theoretical model. The advantage of this expansion over the previous models lies in its generality—any particular force-constant model must have the form given here though not necessarily all its flexibility. The disadvantage lies in the fact that there are many expansion parameters and, therefore, many data are necessary to determine all the constants. The fitting procedure and the parameters used are given in Appendix B.

In this section the results of the lattice model for the phonon dispersion along the Δ, S, P, T, and Σ axes and the density of states are given. The Brillouin-zone notation is that of Kittel,[21] and at the Γ

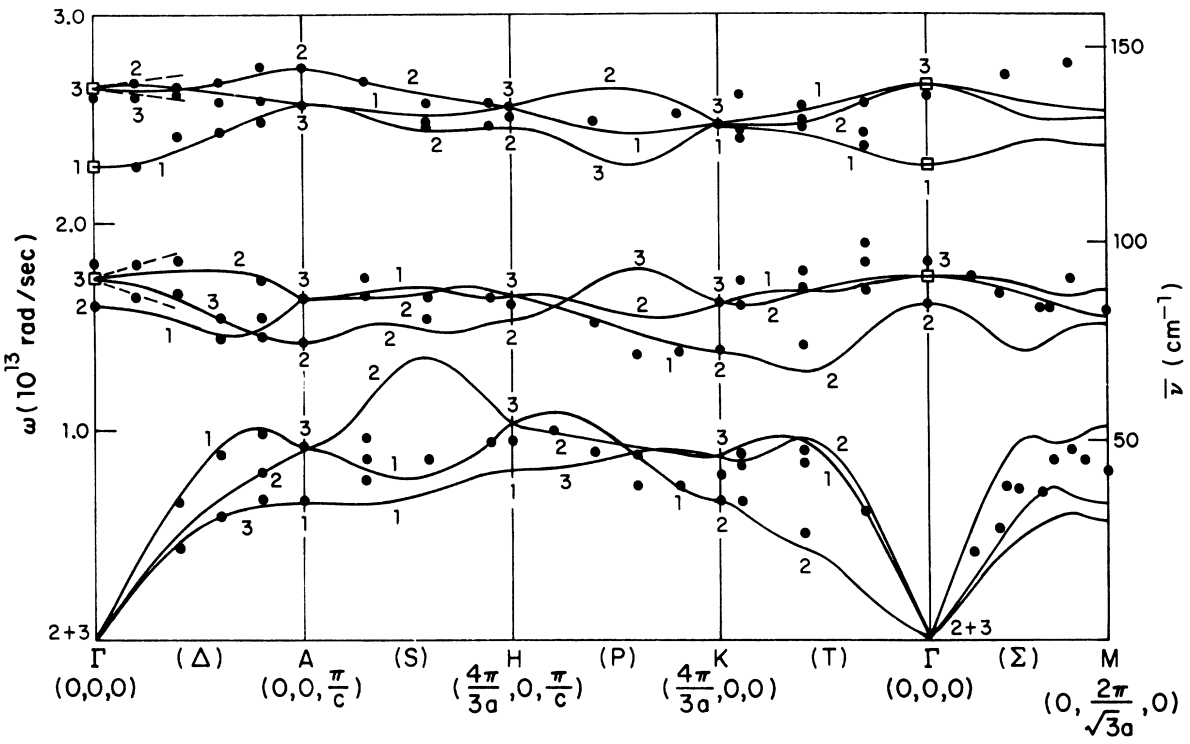

FIG. 3. Phonon dispersion in tellurium along high-symmetry axes of Brillouin zone. The curves are the symmetrized Fourier-expansion lattice-dynamics model; the dots are neutron data (Refs. 1 and 21); the square and slopes are Raman data.

point, symmetry species Γ_1, Γ_2, and Γ_3 correspond to the species A_1, A_2, and E, respectively. The phonon dispersion for the high-symmetry axes is shown in Fig. 3. Neutron data are plotted as solid dots with the Powell and Martel[1] measurements along Δ, S, P, and T, and the Gissler, Axmann, and Springer[22] measurements along Σ. The Raman and infrared data are shown as open squares and linear shifts at the Γ point. The acoustic velocities are fit exactly in the model. Along the Δ axis, where the data are most complete and accurate, the model is heavily weighted to fit these measurements. In the other directions, the Fourier expansion is arbitrarily truncated at third neighbors (see Appendix B) because of the great number of possible parameters and the sketchy data. The fit could be markedly improved in these directions if warranted by better data.

Three regions of the dispersion curves are of particular note. The first is the $\omega_{\Delta_2} > \omega_{\Delta_3}$ band ordering in the upper optical branches near the Γ point. Here, contrary to the previous models, the Raman experiment indicates that the relative $\Delta_2 - \Delta_3$ ordering is the *same* for both optical Γ_3 modes. Alternatively, the assignment $\omega_{\Delta_3} > \omega_{\Delta_2}$ for both Γ_3 optical branches results in a worse fit at the A point for the lower optical modes and a less convergent expansion. The second interesting region is the T_1 and T_2 band crossings of the longitudinal- and fast-transverse-acoustic modes. This is necessitated by the measured elastic constants[8] which indicate that the longitudinal wave is the slower of the two. Third, the fit to the Δ_3 transverse-acoustic branch is much improved over the other models though the near degeneracy with the Δ_2 mode (reported experimentally[1] out to $q_z \sim \pi/2c$) could not be forced. This model implies, therefore, a larger linear wave-vector splitting of the two circularly polarized shear-wave velocities, and consequently a larger acoustical rotary power, [23] than the neutron measurements yield.

The phonon density of states computed by a Monte Carlo selection of about 4000 points in the Brillouin zone is shown in Fig. 4. For all the dispersion and band crossings evident along the high-symmetry axes, it is remarkable that such sharp structure exists in the full-zone density of states. Therefore, it would be inappropriate to assign any of the structure to high-symmetry critical points in the zone. Each of the nine branches remains relatively distinct, isotropic, and dispersionless in a general region of the zone. Phonon modes near the zone center have little effect on the density of states as seen by the low density at the Γ_1 frequency and,

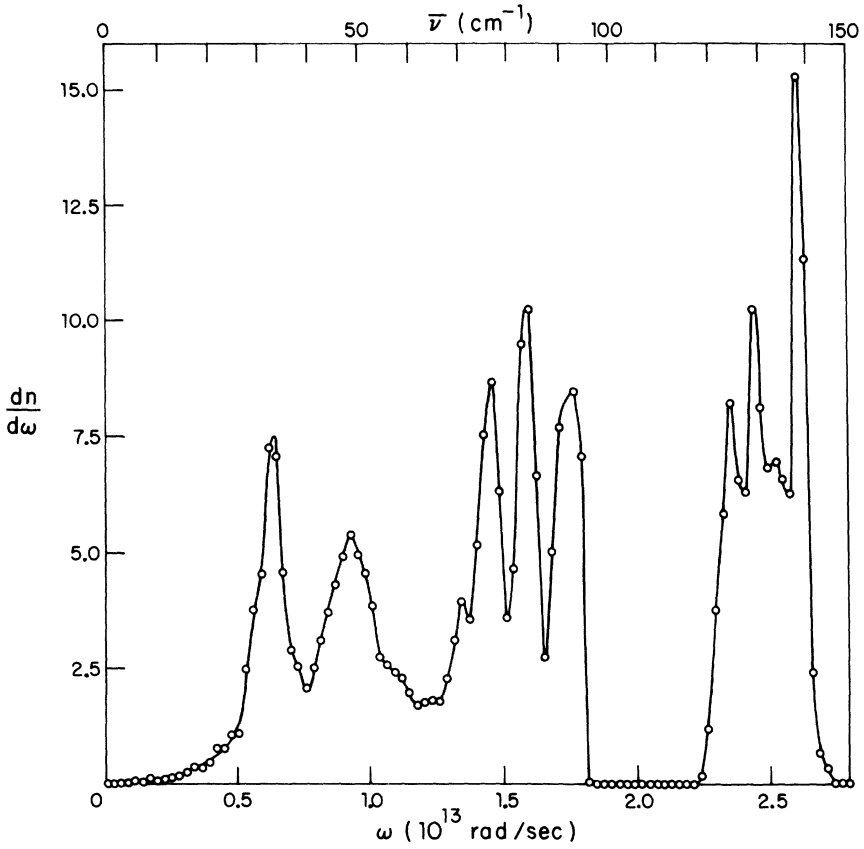

FIG. 4. Phonon density of states for lattice model of tellurium.

of course, in the acoustic region. There is a complete absence of states in the 100–120 cm^{-1} gap and a strong minimum between 55 and 70 cm^{-1}. This latter minimum implies that the second-order Raman structure seen in Fig. 1 does not arise from overtones but is more likely due to combinations of say, the 33-cm^{-1} acoustic branch peak with the 77-, 86-, or 95-cm^{-1} peaks from the lower optical branches.

The Raman spectrum of amorphous tellurium, Fig. 2(d), bears only casual resemblance to the single-phonon density of states of the crystal. The three principal bands observed lack the fine structure of the density of states, and the peak frequencies are all upshifted to rather low-density regions of Fig. 4. Also the sharp low-frequency band in the amorphous material is at variance with the broad acoustic-progenitor interpretation. Therefore it might be concluded that this amorphous tellurium has little short-range order characteristic of the trigonal crystal. However, x-ray scattering[24] does indicate the persistence of helical chains above the melting point of tellurium, and there is apparently no evidence of ring formation such as is observed in selenium amorphous and α monoclinic phases.[25] Thus the interpretation of the Raman spectrum of this laser-melted amorphous tellurium remains open.

The phonon specific heat of tellurium is calculated from the density of states and is shown in Fig. 5. The Debye temperature is ~157 °K as extrapolated from the T^3 portion of the curve at low temperature. This is in good agreement with $\theta_D = 153$ °K measured by P. L. Smith,[26] as it should be since the lattice model is so intimately based on experiment and since the heat capacity is insensitive to the detailed structure.

Note added in proof. The spectrum of Fig. 2(d), attributed to an amorphous state of laser-premelted tellurium, is due to an oxide created at high temperatures. The same characteristic spectrum is obtained from a powdered sample of tetragonal TeO_2. The authors are grateful to B. Cabane for pointing out the improbability of obtaining amorphous tellurium from the melt.

ACKNOWLEDGMENTS

We would like to thank B. M. Powell for a preprint and discussion of his neutron results prior to publication and A. Pinczuk for discussing his unpublished Raman data. Also we have had help from M. S. Dresselhaus on symmetry considerations and calculations and from P. M. Raccah regarding the optical constants of tellurium. We are most grateful to M. J. Redman of Kennecott Copper Corp. and G. Lucovsky and R. C. Keezer of Xerox Corp. for providing the excellent samples. We are indebted to P. H. Keesom for discovering an error in our definition of Debye temperature.

APPENDIX A: FACTORIZATION OF DYNAMICAL MATRIX

As an illustration of the formalism developed in Sec. V, it is instructive to work out the analytically simple examples of the phonon-dispersion relations along the Δ and P axes. Here the dynamical matrix factors into three 3×3 matrices as required by symmetry. Along these axes the phonon wave vector is given by $\vec{q}=((4\pi\delta/3a),\ 0,\ q_z)$, where $\delta=0$ for the Δ axis and $\delta=1$ for the P axis. The only nonvanishing Fourier functions [Eq. (10)] are

$$F_{mn}^{(l)}(A_{1g},q_z)=3C_m^{(l)}(\zeta)\cos\tfrac{4}{3}\pi n\delta\ , \tag{A1a}$$

$$F_{mn}^{(l)}(A_{2u},q_z)=3S_m^{(l)}(\zeta)\cos\tfrac{4}{3}\pi n\delta\ , \tag{A1b}$$

$$F_{mn}^{(l)}(B_{1u},q_z)=3C_m^{(l)}(\zeta)\sin\tfrac{4}{3}\pi n\delta\ , \tag{A1c}$$

$$F_{mn}^{(l)}(B_{2g},q_z)=3S_m^{(l)}(\zeta)\sin\tfrac{4}{3}\pi n\delta\ . \tag{A1d}$$

This greatly reduces the number of matrix elements in Eq. (8) so that the 9×9 dynamical matrix factors into three 3×3's of the form $Z^{(l)}(q_z)$ whose matrix elements are given by

$$Z_{11}^{(l)}(q_z)=\sum_m \gamma_{11}^m(c)C_m^{(l)}(\zeta)\ , \tag{A2a}$$

$$Z_{22}^{(l)}(q_z)=\sum_m[\gamma_{22}^m(c)C_m^{(l+1)}(\zeta)-\gamma_{22}^m(s)S_m^{(l+1)}(\zeta)]\ , \tag{A2b}$$

$$Z_{33}^{(l)}(q_z)=\sum_m[\gamma_{22}^m(c)C_m^{(l+2)}(\zeta)+\gamma_{22}^m(s)S_m^{(l+2)}(\zeta)]\ , \tag{A2c}$$

$$Z_{12}^{(l)}(q_z)=Z_{21}^{(l)*}(q_z)$$

$$=i\sum_m[\gamma_{12}^m(c)C^{(l+2)}(\zeta)-\gamma_{12}^m(s)S_m^{(l+2)}(\zeta)]\ , \tag{A2d}$$

$$Z_{13}^{(l)}(q_z)=Z_{31}^{(l)*}(q_z)$$

$$=-i\sum_m[\gamma_{12}^m(c)C_m^{(l+1)}(\zeta)+\gamma_{12}^m(s)S_m^{(l+1)}(\zeta)]\ , \tag{A2e}$$

$$Z_{23}^{(l)}(q_z)=Z_{32}^{(l)*}(q_z)=\sum_m[\gamma_{23}^m(c)C_m^{(l)}(\zeta)+\gamma_{23}^m(s)S_m^{(l)}(\zeta)]\ . \tag{A2f}$$

Here as seen from (10), the index l is cyclical so $l+3=l$. The γ coefficients are given in terms of the force-constant parameters

$$\gamma_{11}^m(c)=3\textstyle\sum_n\alpha_{11}^{mn}(A_{1g})\cos\frac{4}{3}\pi n\delta\ , \tag{A3a}$$

$$\gamma_{22}^m(s)=3\textstyle\sum_n\alpha_{22}^{mn}(A_{2u})\cos\frac{4}{3}\pi n\delta\ , \tag{A3b}$$

$$\gamma_{12}^m(c)=3\textstyle\sum_n[\beta_{12}^{mn}(A_{1g})\cos\frac{4}{3}\pi n\delta-i\beta_{12}^{mn}(B_{1u})\sin\frac{4}{3}\pi n\delta\ ]\ , \tag{A3c}$$

$$\gamma_{12}^m(s)=3\textstyle\sum_n[\beta_{12}^{mn}(A_{2u})\cos\frac{4}{3}\pi n\delta+i\beta_{12}^{mn}(B_{2g})\sin\frac{4}{3}\pi n\delta\ ]\ , \tag{A3d}$$

$$\gamma_{23}^m(c)=3\textstyle\sum_n\beta_{23}^{mn}(A_{1g})\cos\frac{4}{3}\pi n\delta\ , \tag{A3e}$$

$$\gamma_{23}^m(s)=-3i\textstyle\sum_n\beta_{23}^{mn}(B_{2g})\sin\frac{4}{3}\pi n\delta\ . \tag{A3f}$$

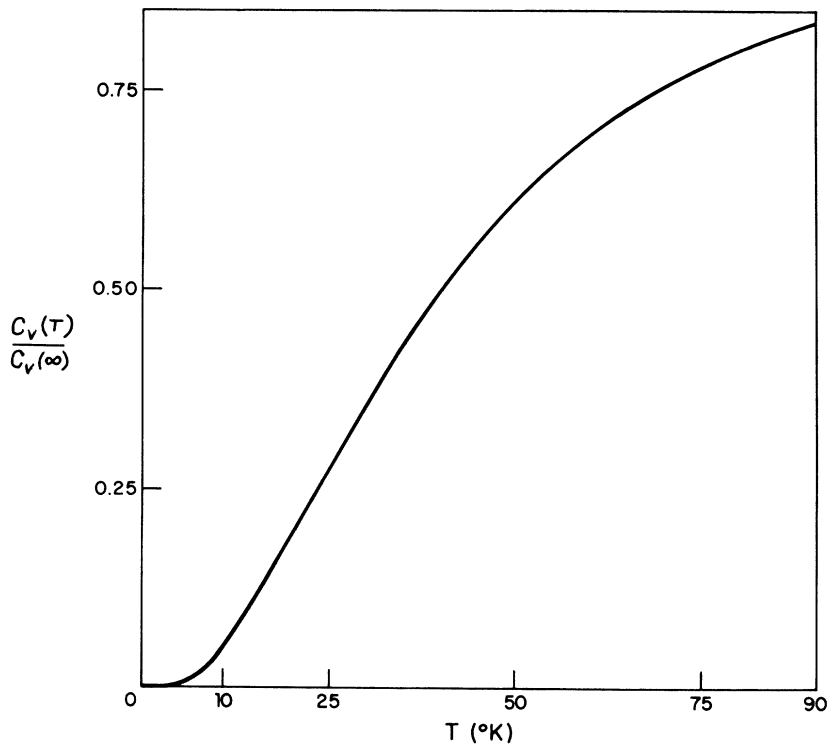

FIG. 5. Phonon specific heat from lattice model of tellurium.

The three matrices $Z^{(l)}(q_z)$ have different properties for the Δ and P axes under time inversion. Along the Δ axis the γ coefficients are purely real, whereas along P some of these coefficients are complex and the $\gamma_{23}^{m}(s)$ term yields an additional q_z dependence. This fundamental difference between the two axes has important consequences for the electronic energy-band problem.[17,18]

The degeneracies of the modes at the Γ, K, A, and H points of the Brillouin zone follow from the values of the Fourier functions [(10) or A1)]. At the Γ and K points, $q_z = 0 = \xi$ so that

$$C_m^{(l)}(0) = \cos\tfrac{2}{3}\pi ml = \begin{cases} 1 & \text{for } ml = 0, 3, 6\cdots \\ -\tfrac{1}{2} & \text{for } ml = 1, 4, 7\cdots \\ -\tfrac{1}{2} & \text{for } ml = 2, 5, 8\cdots \end{cases}, \quad \text{(A4a)}$$

$$S_m^{(l)}(0) = \sin\tfrac{2}{3}\pi ml = \begin{cases} 0 & \text{for } ml = 0, 3, 6\cdots \\ \tfrac{1}{2}\sqrt{3} & \text{for } ml = 1, 4, 7\cdots \\ -\tfrac{1}{2}\sqrt{3} & \text{for } ml = 2, 5, 8\cdots \end{cases}. \quad \text{(A4b)}$$

Thus $C_m^{(0)}(0) = 1$, $S_m^{(0)}(0) = 0$, $C_m^{(1)}(0) = C_m^{(2)}(0)$, and $S_m^{(1)}(0) = -S_m^{(2)}(0)$ which lead to the relations

$$Z_{11}^{(1)}(0) = Z_{11}^{(2)}(0), \quad Z_{22}^{(1)}(0) = Z_{33}^{(2)}(0), \quad Z_{33}^{(1)}(0) = Z_{22}^{(2)}(0),$$

$$Z_{12}^{(1)}(0) = -Z_{13}^{(2)}(0), \quad Z_{13}^{(1)}(0) = -Z_{12}^{(2)}(0), \quad Z_{23}^{(1)}(0) = Z_{23}^{(2)*}(0).$$

Hence $Z^{(1)}(0)$ and $Z^{(2)}(0)$ have degenerate eigenvalues and are compatible with the two-dimensional representations Γ_3 or K_3. Similarly at the A and H points, $q_z = \pi/c$ and $Z^{(0)}(\pi/c)$ and $Z^{(2)}(\pi/c)$ have degenerate eigenvalues compatible with the doublet A_3 or H_3 modes. Note that the conventional symmetry labels 1, 2, and 3 along the Δ and P axes of Fig. 3 correspond to the notation $l = 0$, 2, and 1 of the text.

The matrices $Z^{(0)}(0)$ and $Z^{(1)}(\pi/c)$ for the nondegenerate levels at Γ, K, A, and H factor further into one $\Gamma_1(K_1, A_1$, or $H_1)$ mode and two $\Gamma_2(K_2, A_2$, or $H_2)$ modes. Near the Γ point the $Z^{(0)}(q_z)$ matrix may be transformed into the form

$$\tilde{Z}^{(0)}(q_z) = MZ^{(0)}(q_z)M^{-1} = \begin{bmatrix} (c_{33}^0/\rho)q_z^2 & \epsilon q_z & o(q_z^2) \\ \epsilon^* q_z & \omega_{\Gamma_1}^2 & o(q_z^2) \\ o(q_z^2) & o(q_z^2) & \omega_{\Gamma_2}^2 \end{bmatrix} \quad \text{(A5)}$$

to lowest order in q_z. Here the unitary matrix M which diagonalizes $Z^{(0)}(q_z)$ at the Γ point is

$$M = M^{-1} = \begin{bmatrix} 1 & 0 & 0 \\ 0 & 1/\sqrt{2} & 1/\sqrt{2} \\ 0 & 1/\sqrt{2} & -1/\sqrt{2} \end{bmatrix}. \quad \text{(A6)}$$

The translational and stability constraints, (13) and (14), have been used to derive (A5). These constraints and the measured values of the matrix elements of (A5) yield the following relations between the force-constant parameters of the model:

$$\sum_m \alpha_{aa}^{mn}(A_{1g}) = 0, \quad \text{(A7a)}$$

$$\sum_m \beta_{12}^{mn}(A_{1g})C_m^{(1)}(0) = \sum_m \beta_{12}^{mn}(A_{2u})S_m^{(1)}(0) = 0, \quad \text{(A7b)}$$

$$\sum_m \beta_{23}^{mn}(A_{1g})C_m^{(1)}(0) = 0, \quad \text{(A7c)}$$

$$\sum_m m\,\alpha_{22}^{mn}(A_{2u}) = 0, \quad \text{(A7d)}$$

$$c_{33}^0/\rho = -\tfrac{3}{2}\sum_m (\tfrac{1}{3}mc)^2 \alpha_{11}^{mn}(A_{1g}), \quad \text{(A7e)}$$

$$\omega_{\Gamma_1}^2 = 3\sum_m [\alpha_{22}^{mn}(A_{1g})C_m^{(1)}(0) - \alpha_{22}^{mn}(A_{2u})S_m^{(1)}(0) + \beta_{23}^{mn}(A_{1g})], \quad \text{(A7f)}$$

$$\omega_{\Gamma_2}^2 = 3\sum [\alpha_{22}^{mn}(A_{1g})C_m^{(1)}(0) - \alpha_{22}^{mn}(A_{2u})S_m^{(1)}(0) - \beta_{23}^{mn}(A_{1g})], \quad \text{(A7g)}$$

$$\epsilon = (3i/\sqrt{2})\sum_m (\tfrac{1}{3}mc) \times [\beta_{12}^{mn}(A_{1g})S_m^{(1)}(0) - \beta_{12}^{mn}(A_{2u})C_m^{(1)}(0)]. \quad \text{(A7h)}$$

The eigenvectors associated with the $\tilde{Z}^{(0)}(q_z)$ matrix in the limit $q_z \to 0$ are obtained from the transformation M on the basis functions $U_\mu^{(l)}(0)$, Eq. (2). Thus the normal modes are $U_z^{(0)}(0)$, the longitudinal-acoustic mode of Γ_2 symmetry; $(1/\sqrt{2})[U_-^{(1)}(0) + U_+^{(2)}(0)]$, the symmetric Γ_1 breathing mode; and $(1/\sqrt{2})[U_-^{(1)}(0) - U_+^{(2)}(0)]$, the antisymmetric Γ_2 twist mode. The measured elastic constant is obtained from (B5) to zeroth-order in wave vector,

$$c_{33}/\rho = c_{33}^0/\rho - |\epsilon|^2/\omega_{\Gamma_1}^2. \quad \text{(A8)}$$

To this order only the Raman-active Γ_1 mode affects the elastic constant c_{33} since the interaction with the $\omega_{\Gamma_2}^2$ is quadratic in q_z. This result is a simple illustration of the general theory of the interaction between acoustic and optical modes given in Eq. (20) and by Miller and Axe.[18]

To first order in wave vector, a similar, but parameter-dependent, matrix transforms $Z^{(1,2)}(q_z)$ into the form

$$\tilde{Z}^{(1,2)}(q_z) = \begin{bmatrix} \omega_{E_a}^2 \pm \epsilon_a q_z & \pm\epsilon_{ab} q_z & \pm\epsilon_{ac} q_z \\ \pm\epsilon_{ab}^* q_z & \omega_{E_b}^2 \pm \epsilon_b q_z & \pm\epsilon_{bc} q_z \\ \pm\epsilon_{ac}^* q_z & \pm\epsilon_{bc}^* q_z & ((c_{44}^0/\rho) \pm \epsilon_c q_z)q_z^2 \end{bmatrix} \quad \text{(A9)}$$

near the Γ point. The $\pm$ signs refer to the $l = 1$ or 2 representations. The two zone-center Γ_3 optical

modes are labeled E_a and E_b. Here all the matrix elements have allowed linear wave-vector terms.[6] The linear q_z shifts of the Raman modes measured in this experiment are equated with ϵ_a and ϵ_b. The term $\pm\epsilon_c q_z$ is a first-order spatial dispersion[27] correction to the elastic constant (c_{44}/ρ) of the circularly polarized shear waves $U_{\pm}^{(0)}(0)$. This accounts for the phenomenon of acoustical activity which has been observed in isomorphous α-quartz.[23] The off-diagonal matrix elements represent interactions between the Γ_3 modes similar to Eq. (A8).

The properly symmetrized dynamical matrix $D_{A_1}(\vec{q})$ also factors into a 4×4 and a 5×5 matrix along the T and S axes of the Brillouin zone. Since the set of basis functions (2) have been chosen to manifestly block diagonalize $D_{A_1}(\vec{q})$ along the Δ and P axes, a straightforward transformation into a (x,y,z) representation is required to factorize the matrix along T and S.

APPENDIX B: FITTING PROCEDURE FOR TELLURIUM PHONON-DISPERSION RELATIONS

The experimental measurement of the phonon normal modes over the entire Brillouin zone would make possible a determination of the force-constant parameters, $\alpha_{ij}^{mnp}(\Gamma_k)$ and $\beta_{ij}^{mnp}(\Gamma_k)$, of Eqs. (9a)–(9b). The factorization of the dynamical matrix, Eq. (3), along high-symmetry axes is considered in Appendix A. The simplifications which occur at high-symmetry points and axes make possible a systematic procedure for the evaluation of the force-constant parameters from experimental data.

The analysis of Appendix A shows that simple expressions exist for the Δ and P axes. Along the Δ axis there are six independent parameters for each value of $m\neq0$ plus four parameters for $m=0$. Thus there are 22 parameters for $m\leq3$. Since there is no dependence on n, there is nothing to be gained in fitting the Δ axis by including this parameter. If, however, there are data for both the Δ and P axes, these two axes can be fit independently and in complete generality by taking $n=0$, $m\leq3$ terms (22 constants) for the Δ axis and $n=1$, $m\leq3$ terms (32 constants) for the P axis. There is no need to introduce higher values of n, because only linear combinations given by Eqs. (A3a)–(A3f) enter the matrices for the levels. Thus, an imperfect fit to experimental data would indicate that the convergence is not sufficiently rapid and that $m>3$ terms are also necessary.

For any lower-symmetry axis or a general point in the Brillouin zone, all the terms having E sym-

TABLE II. Fourier coefficients in tellurium in units of $(10^{13}$ rad/sec$)^2$.

	$(n,0,\frac{1}{3}m)$							
	(0,0,0)	$(0,0,\frac{1}{3})$	$(0,0,\frac{2}{3})$	(0,0,1)	(1,0,0)	$(1,0,\frac{1}{3})$	$(1,0,\frac{2}{3})$	(1,0,1)
$\alpha_{11}(A_{1g})$	1.281	−0.462	−0.479	0.024	0.026	−0.391	0.0	0.0
$\alpha_{22}(A_{1g})$	0.950	−0.529	−0.031	−0.077	0.006	−0.318	0.0	0.0
$\beta_{23}(A_{1g})$	0.027	0.496	−0.030	0.242	−0.126	−0.180	0.0	0.0
$\beta_{12}(A_{1g})$	0.191	0.450	−0.084	−0.079	0.083	0.023	0.0	0.0
$\alpha_{22}(A_{2u})$	···	0.082	0.099	−0.111	···	0.054	0.0	0.0
$\beta_{12}(A_{2u})$	···	0.135	−0.007	0.016	···	−0.142	0.0	0.0
$\beta_{12}(B_{1u})$	···	···	···	···	0.142	−0.323	0.0	0.0
$\beta_{12}(B_{2g})$	···	···	···	···	···	−0.214	0.0	0.0
$\beta_{23}(B_{2g})$	···	···	···	···	···	−0.007	0.0	0.0
$\alpha_{13}(E_{1u})$	···	···	···	···	−0.024	0.024	0.0	0.0
$\beta_{13}(E_{1u})$	···	···	···	···	0.046	−0.012	0.0	0.0
$\beta_{22}(E_{1u})$	···	···	···	···	0.162	−0.082	0.0	0.0
$\alpha_{32}(E_{2g})$	···	···	···	···	−0.247	−0.023	0.0	0.0
$\alpha_{13}(E_{2g})$	···	···	···	···	0.241	−0.023	0.0	0.0
$\beta_{11}(E_{2g})$	···	···	···	···	−0.107	0.013	0.0	0.0
$\beta_{22}(E_{2g})$	···	···	···	···	0.022	0.009	0.0	0.0
$\beta_{32}(E_{2g})$	···	···	···	···	−0.325	0.054	0.0	0.0
$\beta_{13}(E_{2g})$	···	···	···	···	0.0	0.0	0.0	0.0
$\alpha_{32}(E_{1g})$	···	···	···	···	···	−0.113	0.0	0.0
$\alpha_{13}(E_{1g})$	···	···	···	···	···	−0.009	0.0	0.192
$\beta_{11}(E_{1g})$	···	···	···	···	···	−0.121	0.0	0.0
$\beta_{22}(E_{1g})$	···	···	···	···	···	−0.018	0.0	0.0
$\beta_{32}(E_{1g})$	···	···	···	···	···	0.124	0.0	0.0
$\beta_{13}(E_{1g})$	···	···	···	···	···	−0.092	0.0	0.0
$\alpha_{13}(E_{2u})$	···	···	···	···	···	0.017	0.0	0.0
$\beta_{13}(E_{2u})$	···	···	···	···	···	0.092	0.0	0.0
$\beta_{22}(E_{2u})$	···	···	···	···	···	−0.005	0.0	0.0

metry enter. There are nine terms for $(na,0,0)$ and 18 terms for a more general point $(na,0,\frac{1}{3}mc)$, $m \neq 0$. Thus there are a total of 63 new terms involving a general point in the Brillouin zone for $n \leq 1$ and $m \leq 3$ for a grand total of 117 constants.

Not all of these 117 parameters are used in the current fit because of insufficient experimental data. In fact, only the 62 nonzero parameters shown in Table II are used and not all of these can be independently specified because of special constraints on the dynamical matrix.

The fitting is done first along the Δ axis where 22 parameters enter for $m \leq 3$ (only those of A_{1g} and A_{2u} symmetry). To determine these parameters, data are available for two velocities of sound,[8] for positions of four modes at Γ and six at A, and for slopes of the $2\Gamma_3$ modes at Γ. In addition, it is necessary to satisfy three constraints associated with the translational symmetry of the entire crystal along the c axis and the stability of the crystal, i.e., no linear terms in ω^2 are allowed for the acoustic Γ_3 mode. This gives a total of 19 conditions to determine 22 constants. Since there are also neutron data available at intermediate points along the axis, the problem is overdetermined and use is made of a least-squares fitting procedure. The resulting fit is shown in Fig. 3. Both the elastic constants and the frequencies of the modes at Γ and at A are fit exactly. The other experiments are fit to within the experimental error. The phonon frequencies along the Δ axis are fit easily, and considerable confidence can be placed in the resulting dispersion curves. The truncation of the expansion seems to be consistent with existing data. The slopes of the dispersion curves at the Γ point are particularly sensitive to truncation because slopes and curvatures weigh higher Fourier components more heavily.

The next step is the fitting of the H- and K-point frequencies using the neutron data. At the present time, these data are less reliable and, indeed, at the H point not all the modes have been identified. From the fitting point of view, all constants having A_{1g}, A_{2u}, B_{1u}, and B_{2g} symmetries enter into the determination of the frequencies of the modes along the P axis. Fitting the dispersion curves along the P axis requires a total of 32 new constants for $n \leq 1$ and $m \leq 3$. Since the current neutron data is incomplete along this axis, there is not sufficient data to evaluate all the constants and only 14 additional constants (namely, those for $n = 1$, $m \leq 1$) were introduced. More neutron data for the entire H-K axis (P axis) would be invaluable in determining the additional parameters.

Lastly, the Γ-K axis (or T axis) is fitted. For this axis, all terms having A_{1g}, A_{2u}, B_{1u}, B_{2g}, E_{2g}, E_{2u} and E_{1g}, E_{1u} enter into the determination of the dispersion curves. Thus a total of 63 additional constants enter. To specify these parameters, one stability constraint, four elastic constants, and the neutron results along any of the low-symmetry axes can be used. In the present fitting only the T axis is considered and with one exception the terms are truncated after $(a,0,0)$ and $(a,0,\frac{1}{3}c)$. The one exception is the term which relates to the c_{13} elastic constant. Because the experiments indicated a large value[8] for this constant, it is felt that at least two terms in the Fourier expansion should be retained. Once again the number of experiments greatly underdetermines the Fourier coefficients. Furthermore, the calculation of the normal modes for a general point in the zone requires the diagonalization of a 9×9 Hermitian matrix. At this time, the accuracy and amount of data for the modes off the Δ axis is not sufficient to motivate a more complete analysis. The model presented here is consistent with most of the known experiments on the phonon-dispersion curves.

---

†Work sponsored by the Department of The Air Force.

[1]B. M. Powell and P. Martel, Proceedings of the Tenth International Conference on the Physics of Semiconductors, 1970, p. 851 (unpublished).

[2]G. Lucovsky, R. C. Keezer, and E. Burstein, Solid State Commun. 5, 439 (1967).

[3]A. Pinczuk, G. Lucovsky, and E. Burstein (private communication).

[4]B. H. Torrie, Solid State Commun. 8, 1899 (1970).

[5]I. Chen and R. Zallen, Phys. Rev. 173, 833 (1968).

[6]A. S. Pine and G. Dresselhaus, Phys. Rev. 188, 1489 (1969).

[7]M. Hulin, Ann. Phys. (Paris) 8, 674 (1963); in *Lattice Dynamics*, edited by R. F. Wallis (Pergamon, New York, 1965), p. 135.

[8]J. L. Malgrange, G. Quentin, and J. M. Thuillier, Phys. Status Solidi 4, 139 (1964).

[9]R. S. Caldwell and H. Y. Fan, Phys. Rev. 114, 664 (1959).

[10]R. Geick and U. Schröder, in *The Physics of Selenium and Tellurium*, edited by W. C. Cooper (Pergamon, New York, 1969), p. 277.

[11]G. Dresselhaus and M. S. Dresselhaus, Intern. J. Quantum Chem. IIS, 333 (1968).

[12]R. Loudon, Advan. Phys. 13, 423 (1964).

[13]A. S. Pine and P. E. Tannenwald, Phys. Rev. 178, 1424 (1969).

[14]W. R. Hunter, J. Opt. Soc. Am. 55, 1197 (1965).

[15]A. Zawadowski and J. Ruvalds, Phys. Rev. Letters 24, 1111 (1970).

[16]R. Shuker and R. W. Gammon, Phys. Rev. Letters 25, 222 (1970).

[17]G. Dresselhaus (unpublished).

[18]M. Hulin, J. Phys. Chem. Solids 27, 441 (1966); M. Picard and M. Hulin, Phys. Status Solidi 23, 563 (1967).

[19]P. B. Miller and J. D. Axe, Phys. Rev. 163, 924 (1967).

[20]M. Lax, in *Lattice Dynamics*, edited by R. F. Wallis (Pergamon, New York, 1965), p. 583.

[21]C. Kittel, *Quantum Theory of Solids* (Wiley, New York, 1963), p. 214.

[22]W. Gissler, A. Axmann, and T. Springer, in *Neutron Inelastic Scattering* (International Atomic Energy Agency, Vienna, 1968), Vol. I, p. 245.

[23]A. S. Pine, Phys. Rev. B 2, 2049 (1970).

[24]R. Buschert, I. G. Geib, and K. Lark-Horovitz, Phys. Rev. 98, 1157 (1955).

[25]G. Lucovsky, in *The Physics of Selenium and Tellurium*, edited by W. C. Cooper (Pergamon, New York, 1969), p. 255; A. Mooradian and G. B. Wright, *ibid.*, p. 269.

[26]P. L. Smith, in *Conférence de Physique des Basses Températures* (Inst. Intern. du Froid, Paris, 1955), p. 281.

[27]D. L. Portigal and E. Burstein, Phys. Rev. 170, 673 (1968).

PHYSICAL REVIEW B VOLUME 4, NUMBER 2 15 JULY 1971

Some Implications of an Expression for the Response of the Electron Liquid*

Flavio Toigo† and Truman O. Woodruff
Department of Physics, Michigan State University, East Lansing, Michigan 48823
(Received 8 February 1971)

The pair correlation function, the screening of a fixed impurity charge, the correlation energy, the cohesive energy of alkali metals, and the plasmon dispersion relation in the small-k limit are calculated using an expression for the dielectric function derived in a previous paper. Results are compared with those obtained from other theories.

I. INTRODUCTION

In a previous paper[1] hereafter referred to as I, we derived an expression [denoted henceforth by $\epsilon_I(k,\omega)$] for the dielectric response function of the electron liquid by means of a momentum-conserving decoupling for the Green's functions involved. (Decoupling by this method is equivalent to imposing the f sum rule on the response function.) This expression is of the form first suggested by Hubbard,[2]

$$\epsilon(\vec{k},\omega)=1+\frac{Q_0(\vec{k},\omega)}{1-G(\vec{k},\omega)Q_0(\vec{k},\omega)}\ , \tag{1.1}$$

where $Q_0(\vec{k},\omega)$ is Lindhard's[3] function. For computational reasons we gave explicit results only for $G(\vec{k},0)$, on the assumption that the term (A3) in I can be neglected. The first noteworthy feature is that it satisfies the compressibility sum rule[4]

$$\lim_{k\to 0} k^2\ \epsilon(\vec{k},0)=\frac{4\alpha r_s}{\pi}\ \frac{C}{C_0}\ , \tag{1.2}$$

with $\alpha=(4/9\pi)^{1/3}$, and k in units of k_F (where C is the compressibility of the electron liquid and C_0 that of the gas) more accurately than do all other available approximations in which the sum rule is not explicitly imposed. This note summarizes the results of calculations based on ϵ_I for some other properties of the electron liquid (i.e., the degenerate gas of interacting electrons): the pair correlation function, the screening of a fixed impurity charge, the correlation energy, the cohesive energy of alkali metals, and the plasmon dispersion in the small-k limit. In addition we show that in the large-k limit, $\epsilon_I(k,\omega)$ includes the effect of a correction to the screening in the random-phase approximation (RPA) previously calculated by Geldart and Taylor.[5]

In the following it is assumed throughout that $G(k,\omega)$ is only weakly dependent on ω so that the dielectric function may be written as

$$\epsilon(\vec{k},\omega)=1+Q_0(\vec{k},\omega)/[1-G(\vec{k})\,Q_0(\vec{k},\omega)]\ , \tag{1.3}$$

with $G(\vec{k})=G(\vec{k},0)$.

This approximation has been widely used in the literature[2,6,7] due to the mathematical difficulties inherent in the computation of the ω dependence of G. The complete expression for $G(k,\omega)$ is given in I.

II. CALCULATION AND RESULTS

A. Pair Correlation Function $g(r)$

It is well known that the pair correlation function

$$g(\vec{r})=[1/N(N-1)]\ \langle\Psi_0|\sum_{i\neq j}\delta\ (\vec{r}+\vec{r}_i-\vec{r}_j)|\Psi_0\rangle \tag{2.1}$$

is related to the static form factor

$$S(\vec{k})=(1/N)\ \langle\Psi_0|\rho_{\vec{k}}^{\dagger}\rho_{\vec{k}}|\Psi_0\rangle \tag{2.2}$$

as follows:

$$g(\vec{r})=\frac{1}{N-1}\sum_{\vec{k}\neq 0}[S(\vec{k})-1]e^{i\vec{k}\cdot\vec{r}}+1\ , \tag{2.3}$$

that is, changing the sum into an integral,